Macroscopic X-ray powder diffraction scanning, a new method for highly selective chemical imaging of works of art : instrument optimization

Macroscopic X-ray powder diffraction scanning - a new method for highly selective chemical imaging of works of art: instrument optimization

Frederik Vanmeert, Wout De Nolf, Steven De Meyer, Joris Dik, and Koen Janssens

Anal. Chem., **Just Accepted Manuscript** • DOI: 10.1021/acs.analchem.8b00240 • Publication Date (Web): 06 Apr 2018

Macroscopic X-ray powder diffraction scanning - a new method for highly selective chemical imaging of works of art: instrument optimization

Frederik Vanmeert,[‡*] Wout De Nolf,[‡†] Steven De Meyer,[‡] Joris Dik[§] and Koen Janssens[‡]

[‡] AXES Research Group, Department of Chemistry, University of Antwerp, Groenenborgerlaan 171, B-2020 Antwerp, Belgium

[§] Department of Materials Science, Delft University of Technology, Mekelweg 2, 2628 CD Delft, the Netherlands

ABSTRACT: In the past decade macroscopic X-ray fluorescence imaging (MA-XRF) has become established as a method for the noninvasive investigation of flat painted surfaces, yielding large scale elemental maps. MA-XRF is limited by a lack of specificity, only allowing for indirect pigment identification based on the simultaneous presence of chemical elements. The high specificity of X-ray powder diffraction (XRPD) mapping is already being exploited at synchrotron facilities for investigations at the (sub)microscopic scale, but the technique has not yet been employed using lab sources. In this paper we present the development of a novel MA-XRPD/XRF instrument based on a laboratory X-ray source. Several combinations of X-ray sources and area detectors are evaluated in terms of their spatial and angular resolution and their sensitivity. The highly-specific imaging capability of the combined MA-XRPD/XRF instrument is demonstrated on a 15th/16th century illuminated manuscript directly revealing the distribution of a large number of inorganic pigments, including the uncommon yellow pigment massicot (*o*-PbO). The case study illustrates the wealth of new mapping information that can be obtained in a noninvasive manner using the laboratory MA-XRPD/XRF instrument.

Over the past ten years macroscopic X-ray fluorescence imaging (MA-XRF) has established itself as an important new tool for imaging of (flat) works of art, delivering significantly more pictorial and material-specific information than traditional X-ray radiography. The resulting elemental distributions provide not only information about the usage of (mostly) inorganic pigments throughout the artwork, but also reveal changes made by the artists during its creative process (pentimenti) or carried out at a later date (e.g. during restorations) and can bring to light completely hidden underpaintings.[1-3] Its successful implementation into a mobile instrument[4] has made MA-XRF available to curators, conservators and conservation scientists inside musea worldwide; many major musea in Europe and the US now use this method. Various MA-XRF instruments have been developed since.[5-10] MA-XRF has contributed to and influenced the process of restoration of well-known masterpieces.[3,11] It has been mostly used on easel paintings,[12] but also on manuscripts[13-15] and stained-glass windows.[16]

A main limitation of MA-XRF is that it yields element-specific rather than pigment-specific distribution maps, rendering direct pigment identification difficult. This poses a problem when pigments with a similar elemental content, such as lead white (cerussite, $PbCO_3$ and/or hydrocerussite, $2PbCO_3.Pb(OH)_2$), red lead (minium, Pb_3O_4), massicot (*o*-PbO), lead tin yellow (type I, Pb_2SnO_4 and type II, $Pb(Sn,Si)O_3$) and Naples yellow (bindheimite, $PbSb_2O_6.PbO$) are used together. They will all contribute to the elemental Pb-L and Pb-M distribution maps obtained by MA-XRF while quite a few of the other elements present (O, C, Si) are not detected because of too low characteristic XRF energies. A second drawback of MA-XRF is the energy-dependent sampling depth. For example, the elemental images corresponding to low energy X-rays such as S-K, K-K, Ca-K convey information limited to the surface of the painting (i.e., the top few μm) while those of, e.g., Cu-K, Pb-L and Hg-L reveal information that can come from much deeper (one to several hundreds of μm below the surface).

X-ray powder diffraction (XRPD) is an important technique for the direct identification of crystalline phases in complex mixtures; it is routinely performed using conventional benchtop diffractometers and more recently with micro (μ-)XRPD instruments inside the laboratory.[17,18] The analysis normally requires removal of (a limited amount of) material from the artwork. Micro destructive sampling of works of art such as precious paintings, in those cases where it is not entirely prohibited, is in practice limited to a small number of locations, e.g., in areas where paint loss already took place or where sampling does not disturb the aesthetic experience of the artwork (e.g. on the edges of a painting). For this reason, the use of noninvasive analogues has become increasingly popular and several portable (p-)XRPD instruments have already been developed.[19] For large immovable objects such as mural paintings and polychrome sculptures or in outdoor environments these instruments might be the only viable alternative to sampling; the long acquisition time (of the order of 20–60 min) required by these devices limits their use to *in situ* point-by-point investigations.

Combining the high specificity of XRD with the high spatial resolution achievable at state-of-the-art synchrotron radiation (SR) facilities leads to significantly more information. In the cultural heritage sector, SR-XRPD imaging at the (sub)microscopic scale has been employed for the study of prehistoric flint-stones,[20] ceramics from the Roman period[21] and porcelain from the Ming dynasty[22], for the identification of various pigments and artist materials[23-25], their degradation products (cadmium yellow[26], chrome yellow[27], vermillion red[28], red lead[29]) and formation of lead soaps[30]. At the macroscopic scale SR-XRPD has been employed for the investigation of Roman wall painting fragments in reflection geometry[31] and in transmission mode for imaging of illuminated manuscript cuttings[32] and Herculaneum papyri fragments[33] and an entire painting[34]. However it remains a tremendous undertaking, both financially and logistically, to guarantee the security and safety of a (precious) work of art during transportation to and its stay at such a large-scale facility.

In order to overcome the above-mentioned limitations, we have developed a combined MA-XRPD/XRF laboratory instrument. In what follows, first a µ-XRPD system with adjustable spatial and angular resolution is discussed. Next, combined MA-XRPD/XRF instruments using different combinations of X-ray sources and area detectors placed in different geometries are evaluated using several figures-of-merit. A sheet of parchment from an illuminated 15th/16th century Book of Tides is used as case study, demonstrating the highly-specific and noninvasive imaging capabilities of the instruments.

MATERIAL AND METHODS

MA-XRPD/XRF setup

In the combined MA-XRPD/XRF systems the X-ray source with beam defining/focusing optic is placed perpendicular to the (essentially two-dimensional) work of art (Figure 1A-B). The single X-ray wavelength required for XRPD is selected from the output of the X-ray tube either via a K_β-filter or a multilayer grating. In this work, powder diffraction signals are exclusively collected in transmission mode by positioning the area detector behind the object and perpendicular to the primary X-ray beam. Reflection-mode scanning MA-XRPD measurements, while quite feasible to realize, are not discussed below. A (semi-transparent) beam stop is used to protect the detector from direct exposure to the primary beam. A Vortex-EX silicon drift detector (SII, Northridge, CA, US) allows for the acquisition of fluorescence radiation. The Vortex detector benefits from a large active area (± 50 mm^2) and has a typical energy resolution of < 165 eV FWHM (at Mn-K_α). The entire instrument remains stationary while the artwork is moved using XYZ motorized stages (Newport Corporation, Irvine, CA, USA; maximum travel ranges: 10 cm × 25 cm × 10 cm). The artwork is positioned by use of a video camera with limited depth of field. The entire scanning operation, including motor movements and acquisitions, is controlled by in-house software. Calibration of various instrumental parameters is performed using a LaB_6 standard for powder diffraction (SRM 660, NIST).

X-ray sources

The low power Mo anode X-ray micro source (RTW-Röntgentechnik Dr Warrikhoff GmbH & Co. KG, D) was equipped with a double polycapillary lens (00-SF-01, X-ray Optics Laboratory, Beijing Normal University, CN) as beam forming optic.[35] By placing a simple K_β-filter (Zr foil, 50 µm, Goodfellow, UK) between the source and polycapillary lens to suppress the unwanted Mo-K_β radiation and part of the background continuum of the X-ray tube, an X-ray micro beam with divergence, monochromaticity and intensity adequate for conducting XRPD experiments can be formed without the need for a more elaborate monochromator.[36]

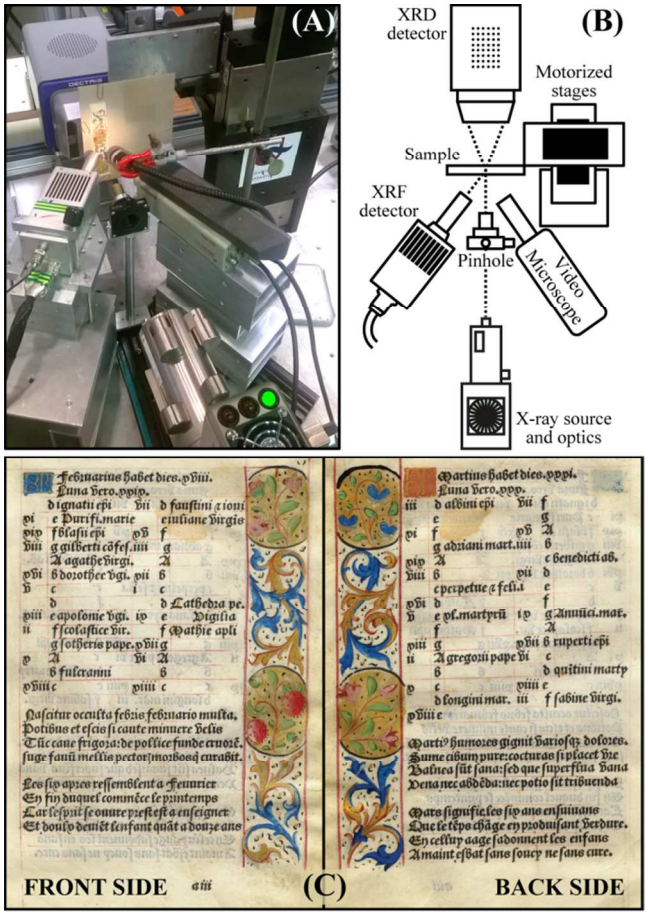

Figure 1 Photograph (A) and schematic (B) of a MA-XRPD/MA-XRF instrument in transmission geometry. (C) Photographs of the front and back side of the 15th/16th c. illuminated sheet of parchment.

The Incoatec microsources (IµS; Incoatec GmbH, D) make use of a Montel optic consisting of two perpendicular mirrors coated with laterally graded multilayers.[37] The Montel multilayer optic simultaneously functions as energy discriminator and as focusing device. The mirrors are kept under low vacuum (several mbar) to prevent degradation of the coating. Focusing optics with large focal distances (between 20 and 40 cm) and limited divergence (< 5 mrad) were chosen to minimize broadening of the diffraction signals. The Incoatec sources can be equipped with several flight tubes to reduce air absorption between optic and sample; a collimator is used to separate the double focused X-ray beam from the unfocused and single focused beams generated by the Montel optics. An Al filter (30 µm) was used with the IµS-Ag^{HB} X-ray source to suppress Ag-L radiation in the primary beam. The technical specifications of the different sources are summarized in Table S-1.

The output focal distance (OFD), focal spot size (FSS) and divergence (Θ) were experimentally determined using wire (Zr or Fe/Cr18/Ni8 wire, 25 µm, Goodfellow) or knife-edge (Zr foil, 25 µm, Goodfellow) scans for all X-ray sources (excluding IµS-Mo). More details about these measurements are provided in the Supporting Information (SI).

Area detectors

A SMART 1000 CCD camera (Bruker AXS Inc., WI, USA) and several hybrid photon counting pixel detectors, PILATUS 100K, PILATUS 200K (Dectris Ltd., CH) and XPAD S140 (ImXPAD SAS, FR) were used. Their characteristics are summarized in Table S-2. Compared to the hybrid pixel detectors, the SMART 1000 CCD has a much smaller pixel size (61 µm) and features a higher detector efficiency at higher X-ray energies (e.g. Mo-K_α and Ag-K_α). Disadvantages of the detector are its long readout time (10 s) and limited dynamic range. Furthermore, to reduce electronic noise the detector chip needs to be cooled down to -45 ºC using a bulky cooling unit (NesLab RTE-140). The hybrid pixel detectors have the benefit of a very short readout time (several ms) and a high dynamic range. The ability to make a selection of the detected photons based on their energy by means of adjustable thresholds makes these detectors practically noise-free. All hybrid pixel detectors in this study make use of Si photodiodes; to increase the sensitivity towards higher energy, different crystal thicknesses were chosen: 320, 500 and 1000 µm for resp. the PILATUS 100K, XPAD S140 and PILATUS 200K cameras. To reduce the relative humidity around the active area, the PILATUS 100K and 200K detectors need to be flushed with dry air or N_2.

Figures-of-merit

Several figures-of-merit were determined for the different X-ray source - detector combinations: spatial resolution, angular resolution, signal-to-noise ratio (SNR), the captured angular range (2θ angles or Q values) and the time between consecutive acquisitions (dead time). The area detector influences the latter four figures-of-merit, while the X-ray source properties affects all with exception of the dead time. The procedures to determine these values can be found in SI.

Illuminated manuscript

The manuscript (private collection) is an excerpt from an illuminated 15th/16th century Book of Tides and features numerous decorations, see Figure 1C. In black ink, a Latin text (accompanied by a French translation) covers most of the parchment. In the margin, colorful vegetal motifs such as strawberries and flowers were applied on both sides. In terms of pigments and materials used as well as its painting style, this folio is very similar to late 15th century folios belonging to Books of Hours of North French/Flemish origin. Similar works are present in for example the Morgan Library and Museum, NYC (e.g., MS M.161 folio 23r, 47r and 80r; http://www.themorgan.org/manuscript/77108 [Accessed 17 March 2018]).[38] The illuminated manuscript has previously been analyzed with a portable Raman-X-ray instrument (PRAXIS) using combined µRaman spectroscopy, µ-XRF and synchrotron µ-XRD,[24] as well as with 3D confocal XRF.[39] Throughout all these studies no visual change to the manuscript folio was noticeable.

Data processing

The XRDUA software package was used for processing of the diffraction data and visualization of the crystalline phase distributions.[40] A detailed overview of the functionality of the XRDUA imaging software is given elsewhere.[41] During a scanning experiment the diffraction data can be analyzed in real-time through regions-of-interest (so-called explorative processing) which provide immediate information about the crystalline contents without prior knowledge of the sample. More elaborate modelling of the data can be performed after data collection (see SI for more details; the data reduction strategy followed is given elsewhere[41]). The intensity scaling parameters in each point of the imaging experiment are used to visualize the spatial distribution of the different compounds.[41] For comparing XRPD data acquired at different wavelengths, it is more convenient to express the diffracted intensity as a function of the energy independent scattering vector (Q), instead of the typically used 2θ-scale. Q-values given throughout this work represent the momentum transfer (i.e. the modulus of the scattering vector given by $Q = 2\pi/d = 4\pi \sin(\theta)/\lambda$). The evaluation of the X-ray fluorescence spectral data was performed with the PyMCA package.[42]

RESULTS AND DISCUSSION

µ-XRPD instrument with variable angular and spatial resolution

By combining a low power Warrikhoff micro source with a double focusing polycapillary lens, a system with an adjustable primary beam size and divergence can be realized. For this instrument the SMART 1000 CCD camera was positioned ~8 cm behind the sample (Figure S-3) and the sample was placed at the OFD of the polycapillary lens. Since this system features variable angular and spatial resolutions, its characteristics will be separately discussed in this section, while the other instruments will be discussed in the following section.

Although it is well documented that the properties of a polycapillary lens are energy dependent,[43] they also depend on the distance between the X-ray source anode and the lens. For optimal output intensity, the X-ray source spot is placed at the designed input focal distance (IFD) of the double focusing polycapillary. By positioning the polycapillary lens closer to the source spot than the optimal IFD of the lens (and thus 'out of focus') the beam is reduced not only in intensity, but also the FSS, Θ and OFD become smaller, as shown in Table 1. Changing from IFD_4 to IFD_1 improves the divergence from 3.7 (1) to 1.4 (2) mrad and the FSS from 422 to 205 µm, at the expense of an appreciable decrease in the focused beam flux (8.5% relative to the intensity at the designed input distance IFD_4). At smaller IFD, the transmission of the polycapillary lens decreases as the X-rays entering the outer capillaries exceed the critical angle for total external reflection and become absorbed. If the IFD is increased beyond IFD_4 (e.g. to IFD_5) a smaller solid angle of the tube output is captured by the lens, leading to a lower output intensity of the optic.

Table 1 Characteristics of the X-ray beam formed by the polycapillary optic (00-SF-01) at different IFD [a]

Label	IFD (cm)	OFD (cm)	Θ (mrad)	FSS (μm)	Relative intensity (%)
IFD_1	4.3 (1)	4.0 (1)	1.4 (2)	205 (2)	8.5 (1)
IFD_2	5.9 (1)	11.4 (1)	1.1 (1)	307 (1)	19.6 (1)
IFD_3	6.9 (1)	17.6 (1)	2.0 (1)	381 (1)	43.4 (1)
IFD_4	7.9 (1)	19.2 (1)	3.7 (1)	422 (1)	100.0 (2)
IFD_5	8.5 (1)	18.7 (1)	3.8 (1)	389 (2)	49.8 (1)

[a] Errors are given in parentheses.

A compromise can be made that combines a limited beam flux with a small beam size and divergence. These latter parameters directly improve the spatial and angular resolution of the μXRPD system. Indeed, the angular resolution improves from about 0.98 to 0.48 nm^{-1} FWHM for the (110) reflection of the LaB_6 standard when changing the distance between the source and lens from IFD_4 to IFD_1 (Figure 2). Since for the analysis of complex mixtures an optimal angular resolution is required, only results from the Warrikhoff X-ray source positioned at IFD_1 relative to the lens are included in the following sections.

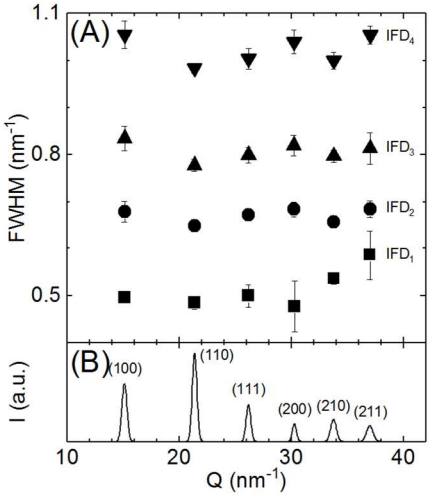

Figure 2 (A) Diffraction peak FWHM versus momentum transfer (Q) for six LaB_6 reflections at different IFD for the Warrikhoff X-ray source and the double focusing polycapillary lens. The results shown are the averages of five to ten measurements with the standard deviations (1s) shown as error bars. (B) Averaged X-ray diffractogram of LaB_6 with Miller indices for the six reflections used in (A).

Comparison of different MA-XRPD systems

Three different geometries were used in which the position of the sample and/or area detector is varied: (A) the sample is placed in the focal point and the detector is positioned in a centered position behind the sample, (B) the distance between sample and the detector is increased and the detector is moved out of the primary beam path and (C) the sample is placed closer to the source and the detector is positioned in the focal point (see Figure S-4). For most configurations a distance between the sample and the area detector was chosen so as to capture a similar Q-range for the three geometries. An overview of the different X-ray source – area detector combinations is given in Table 2 (more details are given in Table S-3).

Table 2 Overview of the different configurations

Configuration	Source	Detector	Geometry	Beam footprint (μm)
1-3	W [a]	1-2:S; 3:X	1:A; 2-3:B	200
4-6		4:P1; 5-6:P2	4,6:B; 5:A	
7	IμS-Mo	S	A	110
8-9	IμS-Cu	P2	8:A; 9:C	8:310; 9:340
10-12	IμS-Ag^{HB}	P2	10:A; 11:B; 12:C	10-11:110; 12:430
13-15	IμS-Cu^{HB}	P2	13:A; 14:B; 15:C	13-14:140; 15:160

[a] using IFD_1. W: Warrikhoff source; S: SMART 1000; X: XPAD S140; P1/2: PILATUS 100K/200K

Spatial resolution

The spatial resolution of the MA-XRPD/XRF system is a measure of the smallest features that can be distinguished in a sample. In geometries A and B the sample is positioned in the focal point of the X-ray optic, resulting in the highest spatial resolution; next to the optic employed, this is mainly determined by the spot size of the X-ray source. With the sources IμS-Mo and IμS-Ag^{HB} a spatial resolution of around 110 μm can be obtained (configurations 7, 10, 11 in Table 2). The IμS-Cu^{HB} source has a slightly larger spot size of 140 μm (configurations 13-14), while the IμS-Cu source produces a focal spot of 310 μm (configuration 8). The configurations with the Warrikhoff X-ray source deliver a spatial resolution of around 200 μm (configurations 1-6). In geometry C the detector rather than the sample is positioned in the beam focus with the sample placed closer to the source. This results in a lower spatial resolution. For configuration 12, using the IμS-Ag^{HB}, the sample is positioned 11.8 cm out-of-focus, increasing the beam footprint to around 430 μm. For configurations 9 and 15 the low Cu-K_α energy requires that only a limited change in the sample position between geometries A and C is needed. This results in a small change in spot size, respectively to 340 and 160 μm for IμS-Cu and IμS-Cu^{HB} (configurations 9 and 15). For all configurations with the Warrikhoff source geometry C is not possible because of the small OFD of the polycapillary lens.

Angular resolution

A high angular resolution is critical to detect small changes in lattice parameters or for unambiguously identifying unknown compounds in a complex mixture. Figure 3A shows that the same geometry does not provide the best angular resolution for each source-detector combination. Geometry A always provides broader diffraction signals compared to B and C. The increase in sample-to-detector distance for geometry B or the intrinsic focusing of the diffraction signals on the detector surface in geometry C improves the angular resolution for these geometries.

Although the SMART 1000 CCD detector has a much smaller pixel size compared to the different hybrid detectors, the point spread function (PSF) of the CCD causes a broadening of the diffraction signals which can be observed when comparing configurations 1 and 5 or 2, 3, 4 and 6. Since the difference between the PILATUS 100K and 200K in this study lies primarily in the size of the active area and the thickness of the silicon photodiodes, no significant change can be seen between the peak widths obtained with both detectors (configurations 4 and 6). The smaller pixel size of 130 μm for the XPAD S140 does results in the best angular resolution

(0.31 – 0.40 nm^{-1}) for all configurations employing the Warrikhoff X-ray source (configurations 1-6).

The angular resolution of the IμS-Ag^{HB} source benefits from the increased distance between sample and detector in geometry B (configuration 11) compared to A (configuration 10), resp. 0.41 – 0.53 nm^{-1} and 0.48 – 0.60 nm^{-1}, but achieves the highest resolution in geometry C (configuration 12) with an improvement of the FWHM to 0.30 – 0.49 nm^{-1}. The increase in peak FWHM values for reflection (211) compared to (100) at higher scattering vectors is mainly ascribed to peak splitting coming from Ag-$K_{\alpha 1}$ and $K_{\alpha 2}$ contributions (see Figure S-5). On the other hand, the IμS-Cu^{HB} source shows a minor difference between geometry A and C (reps. 0.36 – 0.26 nm^{-1} and 0.34 – 0.25 nm^{-1}), but a much better resolution for geometry B with FWHM values around 0.19 nm^{-1} over the entire Q-range (configurations 13-15). Furthermore, the small spot size, low divergence and long wavelength of the IμS-Cu^{HB} source yields the best angular resolution for all tested configurations and geometries. The spot size of IμS-Cu is twice as large compared to IμS-Cu^{HB} and negatively impacts the resolution (configurations 8 and 9). A similar improvement of the angular resolution for geometry B (as seen for IμS-Cu^{HB}, configuration 14) is expected for this source. The decrease in FWHM values with increasing momentum transfer for configurations using Cu-K_{α} results from the decreasing Q-range that is captured by the individual detector pixels. Indeed a single detector pixel at reflection (100) covers a Q-range of 0.20 nm^{-1}, while a pixel for reflection (211) covers a Q-range of 0.07 nm^{-1}. This effect is much less pronounced when a higher energy or a longer sample to detector distance is used (see Figure S-6).

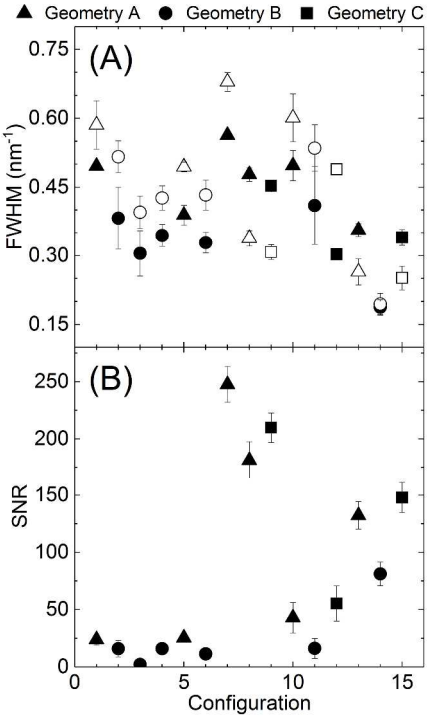

Figure 3 (A) Diffraction peak FWHM for two LaB_6 reflections; (100) (filled symbols) and (211) (empty symbols) obtained with the different configurations. (B) Signal-to-noise ratio normalized to 1 s exposure time. The error bars represent the standard deviation (1s) for 5 to 16 measurements.

The IμS-Mo source combined with the SMART 1000 CCD (configuration 7) gives rise to the largest peak FWHM values. This is expected as geometry A continuously yields the worst angular resolution for all configurations while the PSF of the CCD camera further broadens the diffraction signals.

Signal-to-noise ratio (SNR)

The dwell time per point, which directly affects the total measurement time, should be kept as short as possible so that appreciable areas can be imaged in a reasonable time, but also to limit the dose of radiation the examined sample is exposed to. Reducing the dwell time is only meaningful if the diffraction information remains distinguishable from the background noise. Figure 3B shows the SNR for the different configurations for one second exposure time. The low flux delivered onto the sample by placing the polycapillary lens at IFD_1 relative to the Warrikhoff source results in a low SNR for all configurations (1-6). For the configurations with the Incoatec sources (8-15) the SNR improves with increasing flux.

Although the IμS-Mo and IμS-Ag^{HB} sources have a comparable flux, the SNR is almost six times higher for the former when the same geometry is used (configuration 7 and 10). Since the SMART 1000 CCD is optimized for detecting Mo-K_{α} photons and the conversion of one X-ray photon results in several tens of electrons (~40 electrons per Mo-K_{α} photon) the uncertainty on the obtained intensities is reduced. Similarly configuration 1 has the highest SNR compared to the other Warrikhoff source configurations (3-6) that make use of the hybrid detectors. The limited detection efficiency for the high Ag-K_{α} energy, even for a 1 mm thick active Si layer, combined with the relatively low flux reduces the SNR for configurations 10-12 even more. For configurations 4 and 6 an increase in SNR would be expected due to the two times higher detection efficiency of the 1 mm thick silicon layer of the PILATUS 200K compared to the 100K detector. The deviant behavior of these configurations could be due to the unreproducible alignment of the polycapillary. For geometry B the SNR is always lower compared to A and C. The larger air absorption and more importantly the smaller fractions of the diffraction cones that are intersected by the detector increase the uncertainties on the number of counted photons. For geometries A and C, complete Debye rings are recorded up to Q ≈ 38 nm^{-1}. In this respect it becomes clear that detectors with a large active area will increase the SNR for longer scattering vectors as a larger fraction of their diffraction cones can be captured.

Although the SNR ratios shown in Figure 3B provide a meaningful insight into the advantages of one configuration over the other, the SNR for the different sources will change dramatically depending on the type of sample. More intense Cu sources will be favored for thin samples or samples with limited X-ray absorption, while for highly attenuating or thick materials, selecting the higher Mo-K_{α} or Ag-K_{α} energy will be a more suited approach.

Angular range

The active area of a 2D detector is of importance for capturing a large range of diffraction signals simultaneously. This Q-range depends on the distance and position of the detector to the sample for a specific excitation energy. In most configurations the position of the detector was chosen so as to keep a similar Q-range, independent of the source-detector combina-

tion or geometry, with a maximum momentum transfer of around 38 nm^{-1} (see Table S-3). In the authors' experience it is not necessary to extend this Q-range further as the multitude of reflections at larger scattering vectors leads to peak overlap and for investigations related to paint materials, a distinction between most common pigments can be made at smaller Q values.

Dead time

In addition to the exposure time, there is also a period in between measurements during which no acquisitions can be made (dead time) but which is required for detector readout and motor movements. The dead time is added on top of the acquisition time for each recorded position, sometimes greatly extending the total scanning time. For the scanning setups employing the SMART 1000 CCD detector, its readout time of 10 s represents a major limiting factor. For configurations using the hybrid detectors, the dead time is determined by the motor movements which typically take 2.5 s per start-stop operation. A significant reduction in dead time is possible by employing continuous rather than a start-stop movement of the main motor stage during scanning (so-called sweep mode).

From the figures-of-merit discussed above it becomes clear that configuration 9 is ideally suited for illustrating the potential of MA-XRPD/XRF scanning on the $15^{th}/16^{th}$ c. manuscript. Indeed, for weakly attenuating samples the high SNR and short dead time of this configuration allow for fast imaging of macroscopic areas. Although this configuration features a relatively coarse spatial resolution, this is still more than adequate for visualizing fine decorative details. For more absorbing artefacts or when the angular resolution becomes crucial, respectively configuration 12 or 14 can be used.

Test case: Illuminated $15^{th}/16^{th}$ century manuscript

To illustrate the capabilities of a combined MA-XRPD/XRF scanning system, elemental and compound-specific distributions were simultaneously collected on a $15^{th}/16^{th}$ century illuminated parchment. The entire margin decoration was imaged with configuration 9 over a period of 8.4 hours (map size: 137.6 × 22.8 mm^2; pixel size: 0.4 × 0.4 mm^2; dwell time per point: 0.2 s). Twelve crystalline species were revealed to be present, as shown in Figure 4 (see Table S-4 for PDF codes).

From the photographs it is clear that the gold paint is present on both the front and back side of the sheet of parchment. This is reflected in the gold MA-XRPD distribution showing the cartouches and the gold used for the scrollwork. The Au-M MA-XRF map on the other hand only shows the gold that is used on the front side, i.e. the side of the XRF detector. The use of a monochromatic Cu-K_α excitation energy will only give rise to low energy M-lines of heavy elements such as Au, Hg and Pb. Higher energy L-lines that usually are not so strongly influenced by absorption effects of overlaying layers are not emitted. For the more energetic Fe-K lines a contribution from the back side of the manuscript to the Fe-K MA-XRF map is detected (Figure S-7). A strong Ca-K XRF signal was found throughout most of the manuscript; as visualized with MA-XRPD, this corresponds to calcite ($CaCO_3$) and gypsum ($CaSO_4.2H_2O$). The presence of calcite originates from chalk which was abundantly used during the preparation of parchment. Gypsum has presumably been used as a substrate for a not yet identified organic pink colorant (e.g. in the pink flowers).

The high specificity of the MA-XRPD technique allows for the identification of four Pb-containing pigments: lead tin yellow type I, massicot, hydrocerussite and cerussite. From the Sn-L and Pb-M MA-XRF distributions an indirect identification of lead tin yellow can be made, however the distinction between type I (Pb_2SnO_4) and type II ($Pb(Si,Sn)O_3$) cannot be made. A similar problem arises for hydrocerussite ($2PbCO_3.Pb(OH)_2$), cerussite ($PbCO_3$) and massicot (*o*-PbO), all of which will contribute to the Pb-M MA-XRF distribution. MA-XRPD unambiguously identified lead tin yellow type I to be present in the manuscript, co-localized with massicot and lead white in the green leaves throughout all four cartouches. It is noteworthy that the lead white consists solely of hydrocerussite. Although lead tin yellow type I, besides Naples yellow ($Pb_2(Sb_2O_6(O,OH))$) and orpiment (As_2S_3), was a commonly used yellow in manuscripts, the presence of massicot is noteworthy (see Figure S-8). Massicot, the yellow lead(II) oxide, is mostly found as an impurity to natural or synthesized red lead[44] but has very rarely been used as a yellow pigment on manuscripts or paintings[45]. A different type of lead white, containing both cerussite and hydrocerussite was used for the pink flowers and the white highlights in the cartouches. For the highlights on the strawberries, calcite was added as an extender to the same type of lead white (see Figure S-9).

Two copper carbonates, malachite ($CuCO_3.Cu(OH)_2$) and azurite ($2CuCO_3.Cu(OH)_2$), were used throughout the decorations. A Cu-K_α MA-XRF distribution image could not be obtained because of the too low excitation energy of configuration 9. In order to effectively separate the diffraction peaks of malachite from those of cinnabar (HgS), it was necessary to map the intensity of the isolated malachite (020) reflection (Figure S-10). This shows malachite to be only present in the green leaves (as shown in Figure 4).

The second copper carbonate, azurite, was used for the blue color of the decorative scrollwork and the blue flowers in one of the top cartouches as can be seen in the azurite MA-XRPD map in Figure 4. Azurite is a frequently used blue pigment in European painting.[46] The pigment is of mineralogical origin and is therefore often intermixed with impurities that can be retained during the refinement process. Some of the more common impurities of azurite are malachite, cuprite, and the iron oxides hematite and goethite.[47,48] Although the Fe-K MA-XRF distribution (Figure S-7) closely follows the azurite MA-XRPD distribution, no evidence for hematite or goethite could be found with diffraction. The limited sensitivity of XRPD compared to XRF may be the cause of this. No cuprite and possible only some traces of malachite are found to be present in the azurite-rich areas. Next to the common impurities also the presence of unusual crystallites associated with azurite are of interest in provenance studies. In this case, both barite and quartz are found together with azurite, see Figures S-11 and S-12. The Ba-L MA-XRF distribution is clearly linked to the blue color present on the front side of the parchment while the barite MA-XRPD map correlates very well to the azurite distribution. Other studies have reported barite as an impurity for azurite in paintings[49] and illuminated manuscripts[32,50]. Although barium sulfate has also been used as an artist's pigment, its earliest occurrence as a pigment was not before 1783.[51] Quartz (SiO_2), a less common impurity for azurite,[47,50] shows

some correlation with the azurite distribution (see quartz MA-XRPD), but also appears at first sight, to be strongly linked to the green pigment. However, a more detailed consideration reveals an unresolved overlap between the XRPD peaks of SiO_2 and Pb_2SnO_4 (see Figure S-10D). Unfortunately, there is no isolated XRPD reflection for quartz that can be used to obtain an artefact-free distribution.

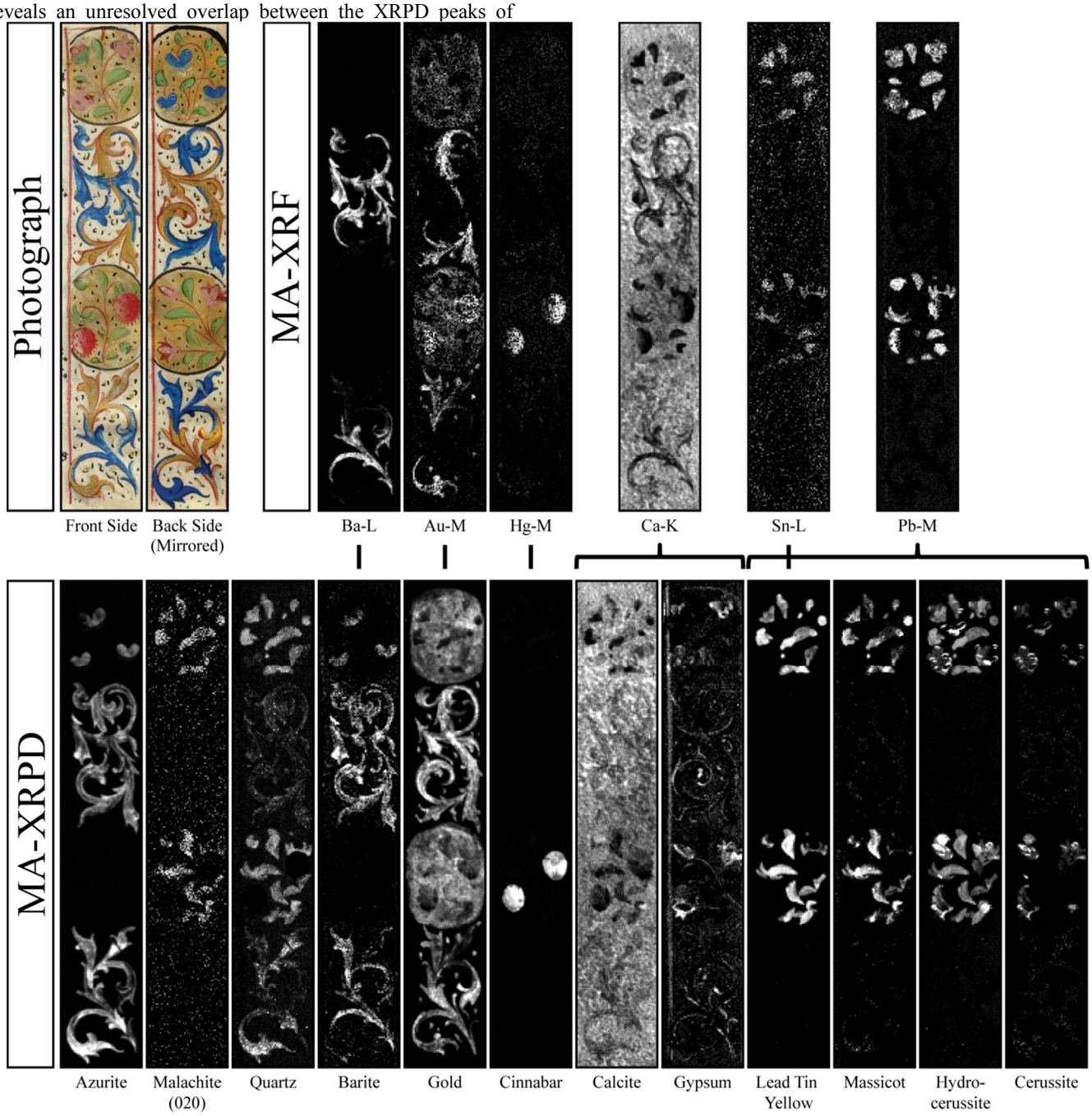

Figure 4 (top left) Photographs of the scanned region for both the front and back side of the illuminated manuscript. Element-specific (top row, MA-XRF) and phase-specific (bottom row, MA-XRPD) distribution images acquired with configuration 9. Whiter tones indicate a higher scaling parameter (MA-XRPD) or fluorescence intensity (MA-XRF). Azurite: $2CuCO_3.Cu(OH)_2$; malachite: $CuCO_3.Cu(OH)_2$; quartz: SiO_2; barite: $BaSO_4$; gold: Au^0; cinnabar: HgS; calcite: $CaCO_3$; gypsum: $CaSO_4.2H_2O$; lead tin yellow: Pb_2SnO_4; massicot: *o*-PbO; hydrocerussite: $2PbCO_3.Pb(OH)_2$ and cerussite: $PbCO_3$. Map size: 137.6 × 22.8 mm^2; pixel size: 0.4 × 0.4 mm^2; dwell time per point: 0.2 s.

CONCLUSIONS

The capabilities of combined MA-XRPD/XRF imaging using laboratory instrumentation have been demonstrated on a sheet of illuminated parchment while employing a dwell time of only 200 ms per point. A large array of crystalline materials was successfully identified and their spatial distribution visualized in a noninvasive manner, providing valuable information on the artistic techniques and materials employed. Not only the different instrumentation (X-ray source, optic and area detector) but also the geometry has an important impact on the performance of MA-XRPD systems. All configurations show different (dis)advantages and the instrument best suited

for a specific analysis will depend on the experimental requirements.

The highly-specific distributions obtained with MA-XRPD greatly complement MA-XRF images of the same artistic artefact. Care should be taken with the interpretation of the MA-XRPD images since overlap of diffraction signals, especially in complex mixtures, can result in incorrect distributions. While the sampling depth for MA-XRF strongly depends on the emitted fluorescence energy and the presence/absence of overlaying layers, for MA-XRPD in transmission mode, information is obtained from all layers as the X-ray beam penetrates the entire layer structure of the manuscript. On the one hand the information present in the compound-specific distributions is therefore much less hampered by absorption from covering layers. On the other hand, a superimposed image from crystalline compounds present on both sides of the manuscript will be obtained, making interpretation of the images sometimes difficult. This aspect is addressed in greater detail in a sequel paper.

An important limitation of the discussed MA-XRPD systems is the restriction on the type of sample that can be analyzed. Since the X-ray beam has to penetrate the entire object this imposes limitations on the thickness of the various covering layers or the type of substrate material that can be present. Furthermore the weight of the entire object needs to be supported by the motorized stages during the scanning operation. Since information is mostly limited to inorganic materials complementary methods that probe organic species such as MA-rFTIR and hyperspectral imaging are required to get a more comprehensive view of painted artworks. Nonetheless MA-XRPD using laboratory instrumentation holds a promising future and recent efforts are being undertaken to construct a mobile MA-XRPD system for on-site examination of (essentially) flat art objects.

ASSOCIATED CONTENT

Supporting Information

Additional information as noted in the text. The Supporting Information is available free of charge on the ACS Publications website.

AUTHOR INFORMATION

Corresponding Author

* Email: frederik.vanmeert@uantwerpen.be

Present Addresses

† Experimental Division, European Synchrotron Radiation Facility, 71 Ave Martyrs, F-38000 Grenoble, France

Notes

The authors declare no competing financial interest.

ACKNOWLEDGMENT

The authors thank the persons involved at Incoatec GmbH, imXPAD SAS and Dectris Ltd. for loaning us some of their products over the past years. We acknowledge financial support from BELSPO (Brussels) S2-ART, the NWO (The Hague) Science4Arts 'ReVisRembrandt' project and GOA Project Solarpaint (University of Antwerp Research Council).

REFERENCES

(1) Dik, J.; Janssens, K.; Van Der Snickt, G.; van der Loeff, L.; Rickers, K.; Cotte, M. *Anal. Chem.* **2008**, *80*, 6436-6442.

(2) Alfeld, M.; Janssens, K.; Rickers, K.; Thijsse, B.; Dik, J. *Zeitschrift für Kunstgeschichte und Konservierung* **2011**, *25*, 157-163.

(3) Alfeld, M.; Van der Snickt, G.; Vanmeert, F.; Janssens, K.; Dik, J.; Appel, K.; van der Loeff, L.; Chavannes, M.; Meedendorp, T.; Hendriks, E. *Appl. Phys. A: Mater. Sci. Process.* **2013**, *111*, 165-175.

(4) Alfeld, M.; Janssens, K.; Dik, J.; de Nolf, W.; van der Snickt, G. *J. Anal. At. Spectrom.* **2011**, *26*, 899-909.

(5) Alfeld, M.; Pedroso, J. V.; Hommes, M. V.; Van der Snickt, G.; Tauber, G.; Blaas, J.; Haschke, M.; Erler, K.; Dik, J.; Janssens, K. *J. Anal. At. Spectrom.* **2013**, *28*, 760-767.

(6) Dooley, K. A.; Conover, D. M.; Glinsman, L. D.; Delaney, J. K. *Angew. Chem.-Int. Edit.* **2014**, *53*, 13775-13779.

(7) Ravaud, E.; Pichon, L.; Laval, E.; Gonzalez, V.; Eveno, M.; Calligaro, T. *Appl. Phys. A: Mater. Sci. Process.* **2016**, *122*, 7.

(8) Alfeld, M.; Mulliez, M.; Martinez, P.; Cain, K.; Jockey, P.; Walter, P. *Anal. Chem.* **2017**, *89*, 1493-1500.

(9) Romano, F. P.; Caliri, C.; Nicotra, P.; Di Martino, S.; Pappalardo, L.; Rizzo, F.; Santos, H. C. *J. Anal. At. Spectrom.* **2017**, *32*, 773-781.

(10) Alberti, R.; Frizzi, T.; Bombelli, L.; Gironda, M.; Aresi, N.; Rosi, F.; Miliani, C.; Tranquilli, G.; Talarico, F.; Cartechini, L. *X-Ray Spectrom.* **2017**, *46*, 297-302.

(11) Van der Snickt, G.; Dubois, H.; Sanyova, J.; Legrand, S.; Coudray, A.; Glaude, C.; Postec, M.; Van Espen, P.; Janssens, K. *Angew. Chem.-Int. Edit.* **2017**, *56*, 4797-4801.

(12) Janssens, K.; Van der Snickt, G.; Vanmeert, F.; Legrand, S.; Nuyts, G.; Alfeld, M.; Monico, L.; Anaf, W.; De Nolf, W.; Vermeulen, M.; Verbeeck, J.; De Wael, K. *Top. Curr. Chem.* **2016**, *374*.

(13) Mosca, S.; Frizzi, T.; Pontone, M.; Alberti, R.; Mbelli, L.; Capogrosso, V.; Nevin, A.; Valentini, G.; Comelli, D. *Microchem. J.* **2016**, *124*, 775-784.

(14) Ricciardi, P.; Legrand, S.; Bertolotti, G.; Janssens, K. *Microchem. J.* **2016**, *124*, 785-791.

(15) Pouyet, E.; Devine, S.; Grafakos, T.; Kieckhefer, R.; Salvant, J.; Smieska, L.; Woll, A.; Katsaggelos, A.; Cossairt, O.; Walton, M. *Anal. Chim. Acta* **2017**, *982*, 20-30.

(16) Van der Snickt, G.; Legrand, S.; Caen, J.; Vanmeert, F.; Alfeld, M.; Janssens, K. *Microchem. J.* **2016**, *124*, 615-622.

(17) Duran, A.; Perez-Rodriguez, J. L.; Jimenez de Haro, M. C. *Anal. Bioanal. Chem.* **2009**, *394*, 1671-1677.

(18) Svarcova, S.; Koci, E.; Bezdicka, P.; Hradil, D.; Hradilova, J. *Anal. Bioanal. Chem.* **2010**, *398*, 1061-1076.

(19) Nakai, I.; Abe, Y. *Appl. Phys. A: Mater. Sci. Process.* **2012**, *106*, 279-293.

(20) Lombardo, T.; Grolimund, D.; Kienholz, A.; Hubert, V.; Worle, M. *Microchem. J.* **2016**, *125*, 254-259.(21) Sciau, P.; Goudeau, P.; Tamura, N.; Dooryhee, E. *Appl. Phys. A* **2006**, *83*, 219-224.

(22) Wang, T.; Zhu, T. Q.; Feng, Z. Y.; Fayard, B.; Pouyet, E.; Cotte, M.; De Nolf, W.; Salome, M.; Sciau, P. *Anal. Chim. Acta* **2016**, *928*, 20-31.

(23) Welcomme, E.; Walter, P.; Bleuet, P.; Hodeau, J. L.; Dooryhee, E.; Martinetto, P.; Menu, M. *Appl. Phys. A: Mater. Sci. Process.* **2007**, *89*, 825-832.

(24) Van der Snickt, G.; De Nolf, W.; Vekemans, B.; Janssens, K. *Appl. Phys. A* **2008**, *92*, 59-68.

(25) Gonzalez, V.; Wallez, G.; Calligaro, T.; Cotte, M.; De Nolf, W.; Eveno, M.; Ravaud, E.; Menu, M. *Anal. Chem.* **2017**, *89*, 13203-13211.

(26) Van der Snickt, G.; Janssens, K.; Dik, J.; De Nolf, W.; Vanmeert, F.; Jaroszewicz, J.; Cotte, M.; Falkenberg, G.; Van der Loeff, L. *Anal. Chem.* **2012**, *84*, 10221-10228.

(27) Monico, L.; Janssens, K.; Hendriks, E.; Vanmeert, F.; Van der Snickt, G.; Cotte, M.; Falkenberg, G.; Brunetti, B. G.; Miliani, C. *Angew. Chem.-Int. Edit.* **2015**, *54*, 13923-13927.

(28) Radepont, M.; de Nolf, W.; Janssens, K.; Van der Snickt, G.; Coquinot, Y.; Klaassen, L.; Cotte, M. *J. Anal. At. Spectrom.* **2011**, *26*, 959.

(29) Vanmeert, F.; Van der Snickt, G.; Janssens, K. *Angew. Chem.-Int. Edit.* **2015**, *54*, 3607-3610.

(30) Cotte, M.; Checroun, E.; De Nolf, W.; Taniguchi, Y.; De Viguerie, L.; Burghammer, M.; Walter, P.; Rivard, C.; Salomé, M.; Janssens, K.; Susini, J. *Studies in Conservation* **2017**, *62*, 2-23.

(31) Dooryhée, E.; Anne, M.; Bardiès, I.; Hodeau, J. L.; Martinetto, P.; Rondot, S.; Salomon, J.; Vaughan, G. B. M.; Walter, P. *Appl. Phys. A* **2005**, *81*, 663-667.

(32) Smieska, L. M.; Mullett, R.; Ferri, L.; Woll, A. R. *Appl. Phys. A* **2017**, *123*, 484.

(33) Brun, E.; Cotte, M.; Wright, J.; Ruat, M.; Tack, P.; Vincze, L.; Ferrero, C.; Delattre, D.; Mocella, V. *Proc Natl Acad Sci U S A* **2016**, *113*, 3751-3754.

(34) De Nolf, W.; Dik, J.; Van der Snickt, G.; Wallert, A.; Janssens, K. *J. Anal. At. Spectrom.* **2011**, *26*, 910.

(35) Kumakhov, M. A.; Komarov, F. F. *Physics Reports-Review Section of Physics Letters* **1990**, *191*, 289-350.

(36) MacDonald, C. A.; Owens, S. M.; Gibson, W. M. *J. Appl. Crystallogr.* **1999**, *32*, 160-167.

(37) Hertlein, F.; Oehr, A.; Hoffmann, C.; Michaelsen, C.; Wiesmann, J. *Particle & Particle Systems Characterization* **2006**, *22*, 378-383.

(38) James, M. R. In *Catalogue of manuscripts and early printed books from the libraries of William Morris, Richard Bennett, Bertram fourth earl of Ashburnham, and other sources, now forming portion of the library of J. Pierpont Morgan.*; Chiswick press: London, 1906, no. 38.

(39) Lachmann, T.; van der Snickt, G.; Haschke, M.; Mantouvalou, I. *J. Anal. At. Spectrom.* **2016**, *31*, 1989-1997.

(40) De Nolf, W.; Janssens, K. *Surf. Interface Anal.* **2010**, *42*, 411-418.

(41) De Nolf, W.; Vanmeert, F.; Janssens, K. *J. Appl. Crystallogr.* **2014**, *47*, 1107-1117.

(42) Sole, V. A.; Papillon, E.; Cotte, M.; Walter, P.; Susini, J. *Spectrochimica Acta, Part B: Atomic Spectroscopy* **2007**, *62*, 63-68.

(43) Bjeoumikhov, A.; Bjeoumikhova, S.; Wedell, R. *Particle & Particle Systems Characterization* **2005**, *22*, 384-390.

(44) Burgio, L.; Clark, R. J. H.; Gibbs, P. J. *J. Raman Spectrosc.* **1999**, *30*, 181-U183.

(45) Kühn, H. In *Artists' Pigments - A Handbook of Their History and Characteristics*, Roy, A., Ed.; Archetype Publications: London, 1993, pp 83-112.

(46) Gettens, R. J.; Fitzhugh, E. W. In *Artists´ Pigments - Handbook of Their History and Characteristics*, Roy, A., Ed.; Archetype Publications: London, 1993, pp 23-36.

(47) Aru, M.; Burgio, L.; Rumsey, M. S. *J. Raman Spectrosc.* **2014**, *45*, 1013-1018.

(48) Burgio, L.; Clark, R. J. H.; Hark, R. R. *Proc Natl Acad Sci U S A* **2010**, *107*, 5726-5731.

(49) Salvado, N.; Buti, S.; Aranda, M. A. G.; Pradell, T. *Analytical Methods* **2014**, *6*, 3610-3621.

(50) Edwards, H. G. M.; Farwell, D. W.; Perez, F. R.; Villar, S. J. *Appl. Spectrosc.* **1999**, *53*, 1436-1439.

(51) Feller, R. L. In *Artists' Pigments - A Handbook of Their History and Characteristics*, Feller, R. L., Ed.; Archetype Publications: London, 1985, pp 47-64.

Authors are required to submit a graphic entry for the Table of Contents (TOC) that, in conjunction with the manuscript title, should give the reader a representative idea of one of the following: A key structure, reaction, equation, concept, or theorem, etc., that is discussed in the manuscript. Consult the journal's Instructions for Authors for TOC graphic specifications.